Supporting information

Molten salt electrolytes with enhanced Li$^+$-transport kinetics for fast-cycling of high-temperature lithium metal batteries

Shuaishuai Yan, # [a] Nan Yao, # [a] Hao Liu, [b] Zheng Zhang, [a] Yang Lu, [a] Zhi Liu, [a] Wenhui Hou, [a] Pan Zhou, [a] Hangyu Zhou, [c] Xiang Chen, [a], * Kai Liu [a], * and Qiang Zhang [a]

[a] State Key Laboratory of Chemical Engineering, Department of Chemical Engineering, Tsinghua University, Beijing 100084, China

[b] Hefei Institute for Public Safety Research, Tsinghua University, Hefei 230601, Anhui, P. R. China

[c] National Academy of Safety Science and Engineering, China Academy of Safety Science and Technology, Beijing 100012, China

# These authors contributed equally to this work.

*Corresponding author.

E-mail address:

xiangchen@mail.tsinghua.edu.cn (X. Chen)

liukai2019@tsinghua.edu.cn (K. Liu).

Experimental section

Preparation of molten salt electrolyte

LiFSI, KFSI, 1,2-dimethoxyethane and propylene carbonate were purchased from Suzhou Duoduo Chemical Technology Co. and used as received. 1-Butyl-3-methylpyrrolidinium bis(fluorosulfonyl)imide ($\geq$ 98%) was purchased from Shanghai Aladdin Biochemical Technology Co. CsFSI was synthesized through replacement reaction of KFSI and CsF (99%, Macklin) in ethanol. The binary and ternary molten salts were prepared by mixing the alkali salts with specific molar ratios, which is consistent with the composition with the lowest eutectic temperature reported in literatures. Li–K (LiFSI:KFSI=41%:59%), Li–Cs (LiFSI:CsFSI=47%:53%) and Li–K–Cs (LiFSI:KFSI:CsFSI=30%:35%:35%) homogeneous mixtures obtained by stirring the salts in a glass bottle at 150°C until a transparent liquid formed.

Material characterizations

Differential scanning calorimetry (DSC) was conducted on a TA Q100. The thermal properties were collected under N_2 atmosphere with a fixed heating rate of 10°C min^{-1}. The flammability of electrolytes was evaluated by igniting a certain mass of the electrolyte with a butane torch. The ignition time was ~1 s. Fourier transform infrared spectroscopy (FTIR) was performed on a Nicolet iS50. Nuclear magnetic resonance (NMR) experiments were carried out on a Bruker AVANCEIII-400M for ^{7}Li spectra. Scanning electron microscope images were collected on a JSM-7401 and atomic force microscope (AFM) images were obtained on an Oxford Instruments Cypher VRS. The CEI layers on NCM811 particles were characterized by a JEM-2100 Plus transmission electron microscope. X-ray photoelectron spectroscopy (XPS) was applied to analyze the SEI/CEI composition on a Shimadzu/Kratos AXIS SUPRA$^+$. Time of flight secondary ion mass spectrometry (TOF-SIMS) was performed on an ION-TOF GmbH TOF.SIMS 5-100 with a sputtering rate of 0.25 nm s^{-1}. Inductively coupled plasma optical emission spectrometer (ICP-OES) was conducted on an Agilent 5800 ICP-OES to detect the concentration of Al^{3+} and transition metal ions in electrolytes.

Molecular dynamics simulations

MD simulations were conducted using the LAMMPS code and the OPLS-AA force field.[1-3] Li-K, Li-Cs, and Li-K-Cs models containing 410 LiFSI and 590 KFSI, 470 LiFSI and 530 CsFSI, 300 LiFSI, 350 KFSI, and 350 CsFSI, respectively, were constructed. The parameters of cations and FSI⁻ were obtained from Jensen *et al.*[4] and Lopes *et al.*,[5] respectively, where the ion charge is scaled by 0.9. The initial atomic coordinates were generated with Packmol[6] program and the solvation structures were visualized by VESTA.[7]

Temperatures of 443.15, 493.15, 543.15, 593.15, and 643.15 K were set, and the conductivity at each temperature was calculated. The periodic boundary conditions were applied in all three directions for all simulations. A cutoff of 12 Å was used for both van der Waals interactions and long-range correction (particle–particle particle-mesh) of Coulombic interactions. The time step was fixed to be 1 fs. All models were first equilibrated in NPT ensemble using the Parrinello–Rahman barostat for 2 ns to maintain a setting temperature and a pressure of 1 atm with time constants of 0.1 and 1 ps, respectively.[8] After that, the electrolytes were heated from the setting value to a value higher by 60 K within 0.5 ns, and maintained at the high temperature for 1 ns, followed by being annealed within 0.5 ns. Subsequently, the models were equilibrated at the setting temperature in NPT ensemble for another 4 ns. A 7 ns produciton run was finally conducted in NVT ensemble under Nose–Hoover thermostat.[9,10] Only the final 5 ns was used to calculate conductivities and analyze solvation structures.

The conductivities (σ) were calculated by the Nernst–Einstein equation:

$$\sigma = \frac{Z_c^2 e^2 C}{k_B T} D_\sigma \tag{S1}$$

$$D_\sigma = \lim_{t \to \infty} \left[\frac{1}{2dt} \langle \left(\frac{1}{N} \sum_{i=1}^{N} \mathbf{r}_i(t) \right)^2 \rangle \right] \tag{S2}$$

where σ, k_B, T, Z_c, e, C, D_σ, d, N, and $\mathbf{r}_i(t)$ are the ionic conductivity, Boltzmann constant, temperature, valence state of the carriers, electron charge, carrier concentration, charge diffusion coefficient, diffusion dimension, the number of the

3

diffusing ions, the displacement of atom i after time t, respectively.

Electrochemical characterization

The ionic conductivity (σ) was calculated from the electrochemical impedance spectroscopy measurements of stainless steel (SS)/SS symmetric cells on a PARSTAT MC electrochemical workstation over a frequency range from 0.1 to 100 kHz. The specific σ values were obtained according to the following equation:

$$\sigma = L/(S \cdot R) \tag{S3}$$

where L represents the thickness, S represents the contact area, and R is the bulk ohmic resistance obtained by EIS.

Li/Li symmetric cells were assembled and measured according to the Bruce-Vincent method to obtain the Li^+ transference number.[11] The polarization voltage (ΔV) was fixed at 10 mV. The t_+ values were calculated according to the following equation:

$$t_+ = I_s(\Delta V - I_0 R_0)/(I_0(\Delta V - I_s R_s)) \tag{S4}$$

where I_s and I_0 are the steady-state and initial currents, respectively. R_s and R_0 are the steady-state and initial interfacial resistance, respectively.

The Tafel curves and exchange current density values were obtained from cyclic voltammetry tests of Li/Li cells (-0.1 V $\sim$ 0.1 V) on a CHI760e electrochemical workstation with a scan rate of 1 mV s^{-1}. For linear sweep voltammetry tests, Al/Li cells were assembled and tested at a scan rate of 5 mV s^{-1}. For the Al corrosion tests of Al/Li cells, the voltage was held at 4.5 V for 10 h. For the potentiostatic polarization tests of NCM811/Li cells, constant current charging was firstly conducted at 0.1 C to reach 4.3 V. Then, the applied voltage was increased stepwise from 4.3 V to 6.1 V with intervals of 0.2 V. Each step was held for 3 h.

Battery assembly and tests

All tests were carried out in 2032-type coin cells. All cells were assembled in an argon-filled glove box ($O_2 < 0.01$ ppm, $H_2O < 0.01$ ppm). The glass fiber separator was used for cells running at 100°C and the Celgard 3501 separator was used for cells running at 80°C. The amount of the electrolyte was 70 µL for all cells. All the electrochemical tests were conducted on a Lanhe LAND CT2001A testing system at

80°C unless otherwise specified. The Cu/Li cells underwent three formation cycles at 0.1 mA cm^{-2}. The depositing time was 1 h and the stripping cut-off voltage was 0.5 V. The NCM811 cathode is prepared by mixing NCM811 active material, Super P, and polyvinylidene difluoride binder with a weight ratio of 90:5:5 in N-methylpyrrolidone. All the cathodes were dried at 100°C under vacuum for 12 h before cell assembly. For the NCM811/Li cells, an Al-coated cathode case with an additional Al foil was used to avoid the corrosion behavior of FSI$^-$ on stainless steels. The NCM811 cathodes were cut into 12 mm diameter and the corresponding Li anodes were cut into 14 mm diameter. There are two types of NCM811 cathodes (1 C = 200 mA g^{-1}) with different mass loadings. The NCM811/Li half cells were composed of ~ 3 mg cm^{-2} NCM811 cathode and 450 μm Li foil. The NCM811/Li full cells were composed of ~ 9.5 or 14 mg cm^{-2} NCM811 cathode and 40 μm Li foil. All cells were allowed to rest at 80°C for 12 h before charge-discharge tests.

DSC tests

Differential scanning calorimetry tests were conducted on a TA Q100 to study the thermal stability and heat generation of the individual electrolyte, the mixture of cycled Li and electrolyte. The cycled Li was obtained from NCM811 (3 mg cm^{-2})/Li (40 μm) half cells running after 25 cycles. The Li foil was washed with DME and then dried under vacuum. 3.5 mg Li sample and 8 mg fresh electrolyte were sealed in a crucible and heated to 450°C to record the heat flow.

a
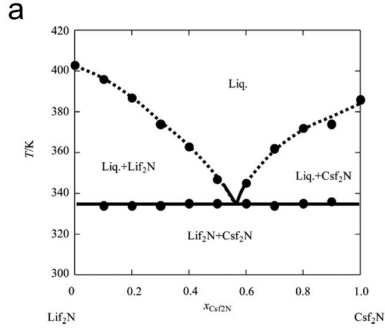
System	Composition	T (K)
LiFSA–NaFSA	$x_{Li} = 0.40$, $x_{Na} = 0.60$	349
LiFSA–KFSA	$x_{Li} = 0.41$, $x_{K} = 0.59$	341
LiFSA–RbFSA	$x_{Li} = 0.38$, $x_{Rb} = 0.62$	337
LiFSA–CsFSA	$x_{Li} = 0.47$, $x_{Cs} = 0.53$	335
NaFSA–KFSA	$x_{Na} = 0.56$, $x_{K} = 0.44$	334
NaFSA–RbFSA	$x_{Na} = 0.50$, $x_{Rb} = 0.50$	328
NaFSA–CsFSA	$x_{Na} = 0.47$, $x_{Cs} = 0.53$	325
KFSA–RbFSA	$x_{K} = 0.31$, $x_{Rb} = 0.69$	354
KFSA–CsFSA	$x_{K} = 0.54$, $x_{Cs} = 0.46$	336
RbFSA–CsFSA	$x_{Rb} = 0.65$, $x_{Cs} = 0.35$	360

b
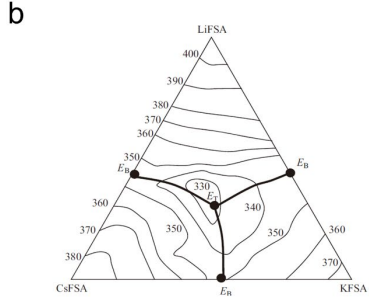
System	Composition	T (K)
LiFSA–NaFSA–KFSA	E: $x_{Li} = 0.30$, $x_{Na} = 0.40$, $x_{K} = 0.30$	318
LiFSA–NaFSA–CsFSA	E: $x_{Li} = 0.30$, $x_{Na} = 0.40$, $x_{Cs} = 0.30$	311
LiFSA–KFSA–CsFSA	E: $x_{Li} = 0.30$, $x_{K} = 0.35$, $x_{Cs} = 0.35$	312
NaFSA–KFSA–CsFSA	E: $x_{Na} = 0.40$, $x_{K} = 0.25$, $x_{Cs} = 0.35$	309

Fig. S1 (a) Phase diagram of LiFSI–CsFSI binary system and corresponding optimal eutectic composition. (b) Phase diagram of LiFSI–KFSI–CsFSI ternary system and corresponding optimal eutectic composition.[12-14]
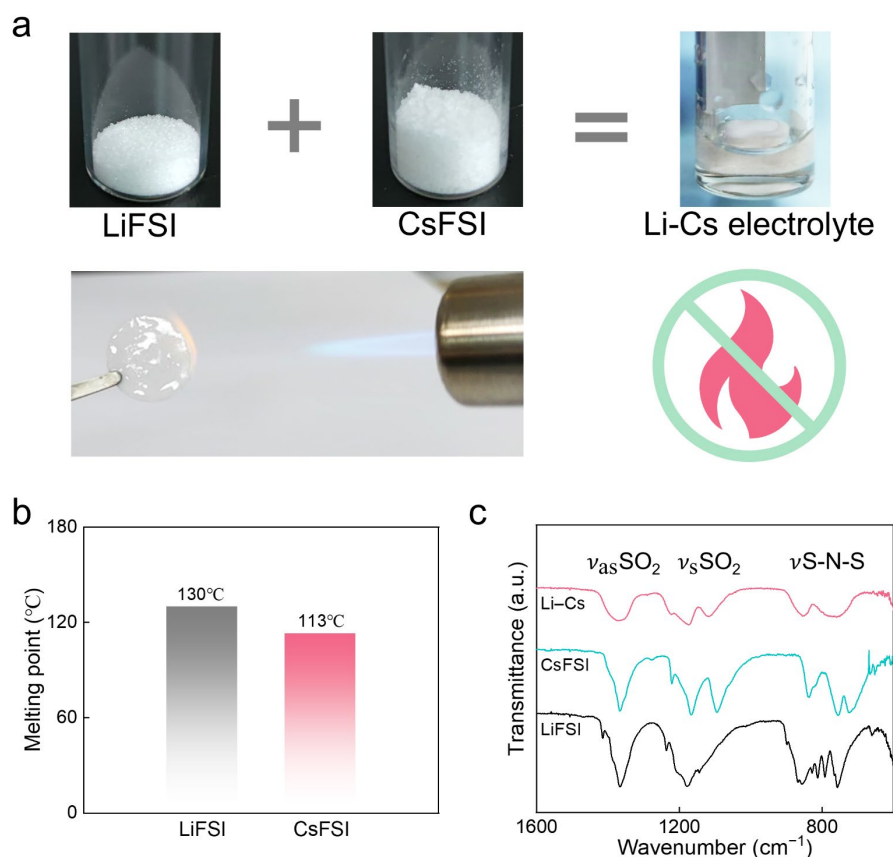
Fig. S2 (a) Preparation process and non-flammability of Li–Cs electrolyte. (b) Melting points of LiFSI and CsFSI salts. (b) FTIR spectra of LiFSI, CsFSI and Li–Cs electrolyte.

Note: LiFSI was applied as conducting salts in molten salt electrolytes for lithium-based batteries due to its relatively low melting point (130°C), good thermal stability and wide electrochemical window (Fig. S2a). KFSI or CsFSI with different sizes of alkali metal cation and low melting points were usually added to form low eutectic-temperature mixtures (Fig. S2b). FTIR tests were carried out on the Li–Cs electrolyte (47 mol% LiFSI and 53 mol% CsFSI) in Fig. S2c. The vibrational peaks at around 1370 cm^{-1}, 1170 cm^{-1} and 780 cm^{-1} are assigned to SO_2 asymmetric stretching mode, SO_2 symmetric stretching mode and S–N–S stretching mode, respectively.[15] Compared to neat LiFSI and CsFSI salts, the intensities of all three peaks of Li–Cs electrolyte decrease and the peak shapes become rounding, suggesting reduced internal orientation of the binary mixture.
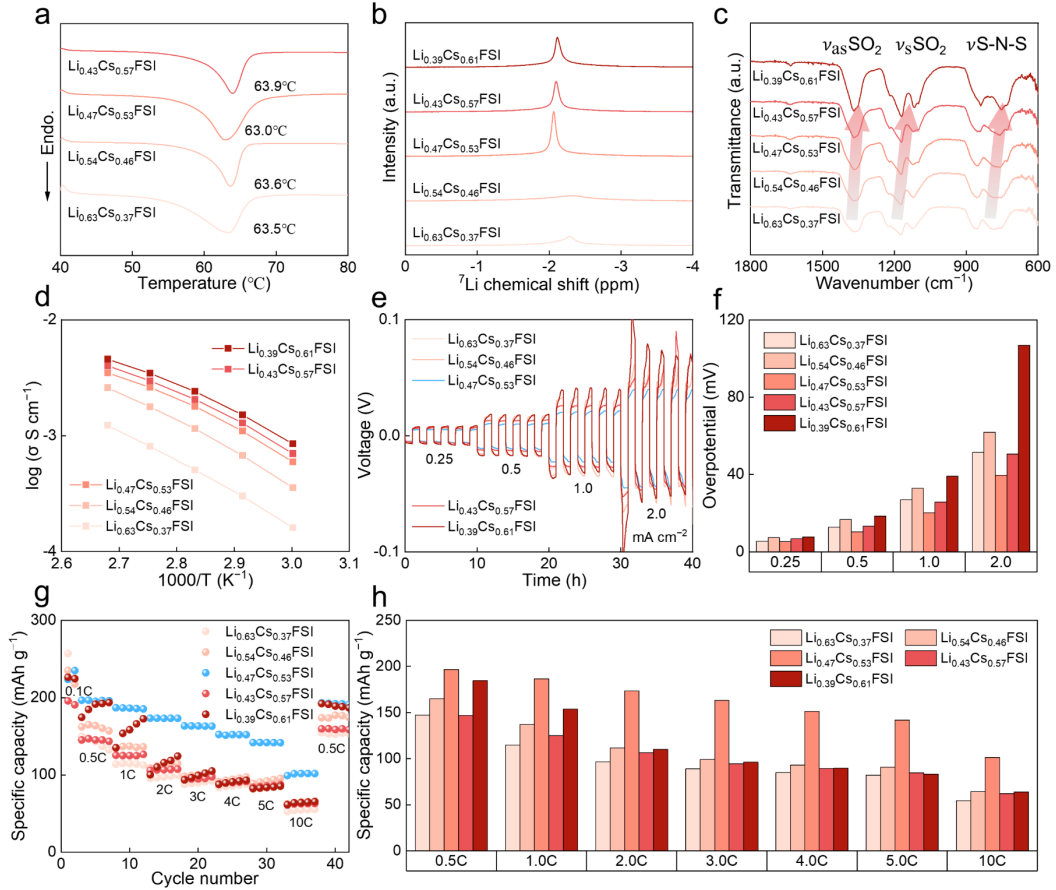
Fig. S3 (a) DSC curves, (b) ^{7}Li NMR spectra, (c) FTIR spectra, and (d) ionic conductivities of Li–Cs electrolytes with varying molar ratios. (e) Rate performance of Li/Li symmetric cells from 0.25 mA cm^{-2} to 2.0 mA cm^{-2} and (f) corresponding overpotential values at different current densities. (g) Rate performance of NCM811/Li cells from 0.5 C to 10 C and (h) corresponding specific capacity values at different rates.

Note: The physicochemical properties and battery performance of Li–Cs electrolytes with varying salt ratios were systematically investigated. As DSC results shown in Fig. S3a, the Li$_{0.47}$Cs$_{0.53}$ electrolyte exhibits the lowest melting point of 63.0°C, followed by Li$_{0.63}$Cs$_{0.37}$ (63.5°C), Li$_{0.54}$Cs$_{0.46}$ (63.6°C) and Li$_{0.43}$Cs$_{0.57}$ (63.9°C). Choosing a lower T_m to operate the battery helps alleviate the thermal decomposition of alkali metal salts. The Li$^+$ chemical environment in different molten salts was examined by NMR in Fig. S3b. Compared to Li$_{0.63}$Cs$_{0.37}$ (−2.29 ppm), Li$_{0.54}$Cs$_{0.46}$ (−2.34 ppm), Li$_{0.43}$Cs$_{0.57}$ (−2.10 ppm) and Li$_{0.39}$Cs$_{0.61}$ (−2.11 ppm), the ^{7}Li signal of deep-eutectic Li$_{0.47}$Cs$_{0.53}$ electrolyte shifts downward to −2.06 ppm and has the narrowest peak width at half-height. This result indicates that the Li$_{0.47}$Cs$_{0.53}$ electrolyte has the most relaxed Li$^+$ coordination environment among the five analogues. Besides, FTIR tests were carried out to

determine the chemical environment of FSI⁻ anionic species in Fig. S3c. All three vibrational peaks of FSI⁻ anions show a red shift with the increase of CsFSI content in molten salts, demonstrating the weakened interaction between FSI⁻ anions and surroundings. Fig. S3d shows that the total ionic conductivity increases with the increase of CsFSI content in molten salts. The $Li_{0.63}Cs_{0.37}$ electrolyte with minimal CsFSI content exhibits the lowest conductivity and $Li_{0.39}Cs_{0.61}$ electrolyte with maximum CsFSI content exhibits the highest conductivity. Based on the FTIR and conductivity results, we can find that the addition of CsFSI is beneficial for increasing the movement freedom of FSI⁻ anions, thus achieving a higher ionic conductivity. Because only the portion of the current carried by Li^+ ions matters in lithium-based batteries, so, we further investigate the rate performance of Li/Li symmetric cells and NCM811/Li cells with varying LiFSI–CsFSI binary electrolytes. In Fig. S3e and f, the Li/Li cell using $Li_{0.47}Cs_{0.53}$ electrolyte shows the lowest overpotential as the current density increases from $0.25\,\mathrm{mA\,cm^{-2}}$ to $2.0\,\mathrm{mA\,cm^{-2}}$. In Fig. S3g and h, the NCM811/Li cell using $Li_{0.47}Cs_{0.53}$ electrolyte shows the highest specific capacity in the range from 0.5 C to 10 C. The above battery results indicate that although the addition of CsFSI can improve the total ionic conductivity, excessive CsFSI dilutes the overall Li^+ concentration, thereby exacerbating internal polarization and deteriorating battery performance. As for the poor performance of $Li_{0.63}Cs_{0.37}$ and $Li_{0.54}Cs_{0.46}$ electrolytes, it is due to the insufficient CsFSI that can not effectively weaken the cation-anion interaction inside the mixture, resulting in a low conductivity. In conclusion, $Li_{0.47}Cs_{0.53}$ electrolyte with the most relaxed Li^+ coordination environment and moderate Li^+ concentration demonstrates the best rate performance with fast Li^+- transport kinetics.
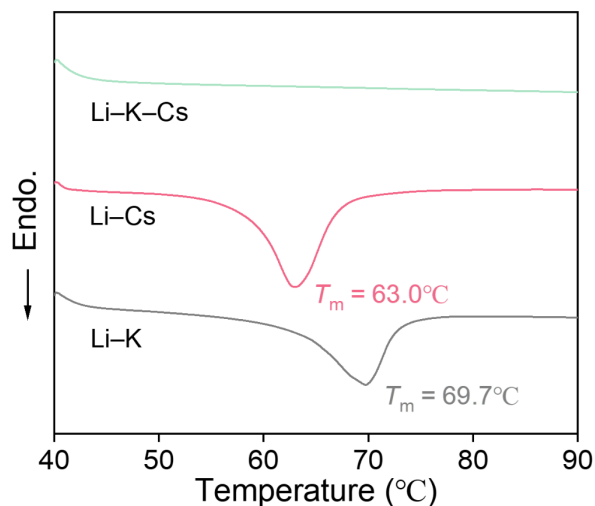
Fig. S4 The melting temperature values of three molten salts.

Note: The measured melting points of Li–K and Li–Cs molten salts are close to the reported values in literatures.[13] As for Li–K–Cs, we don't observe an obvious endothermic peak during the whole heating process from 40°C to 90°C. This is due to the increase in entropy of Li–K–Cs system, which leads to strong resistance to crystallization. Based on previous research, we have determined that the melting point of Li–K–Cs is 45°C.[14]
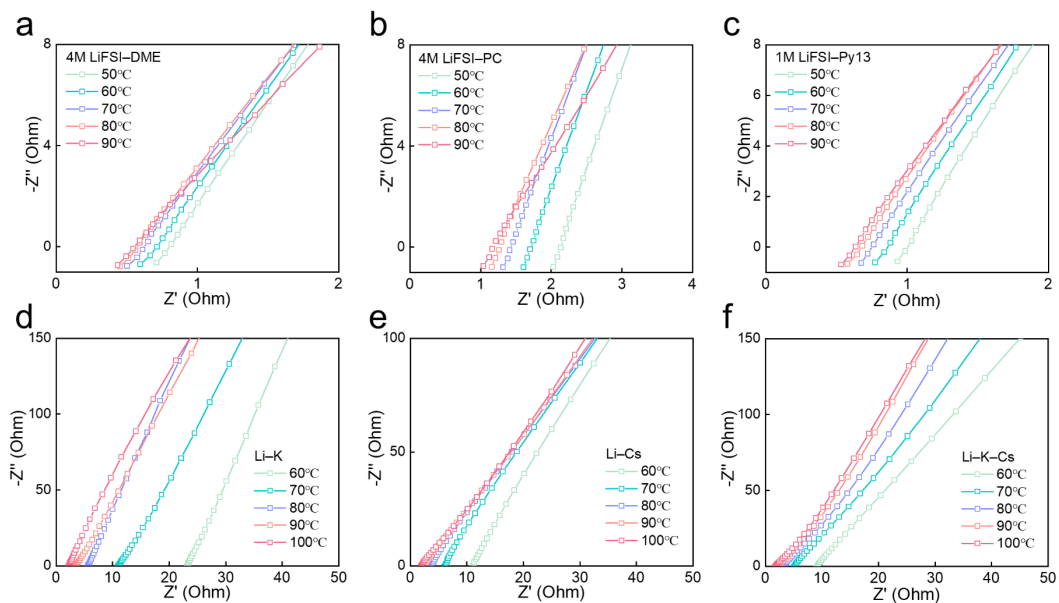
Fig. S5 Temperature-dependent impedance of SS/SS cells with (a) 4M LiFSI–DME, (b) 4M LiFSI–PC, (c) 1M LiFSI–Py13, (d) Li–K, (e) Li–Cs, and (f) Li–K–Cs electrolytes in Nyquist plots.
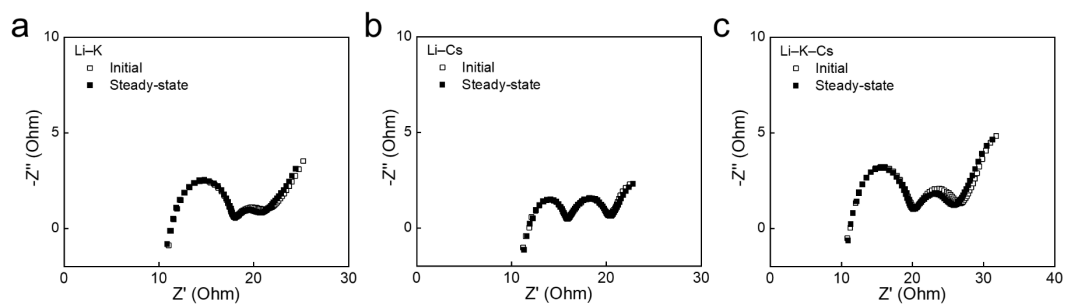
Fig. S6 The initial and steady-state impedance of (a) Li–K, (b) Li–Cs, and (c) Li–K–Cs electrolytes in Li$^+$ transference number measurements.
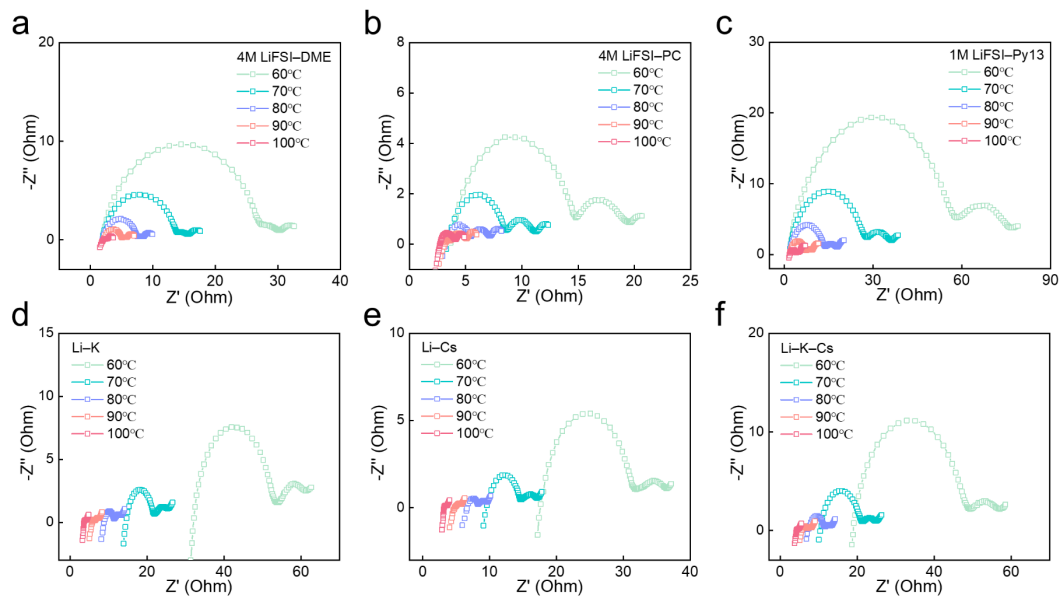
Fig. S7 Temperature-dependent impedance of Li/Li cells with (a) 4M LiFSI–DME, (b) 4M LiFSI–PC, (c) 1M LiFSI–Py13, (d) Li–K, (e) Li–Cs, and (f) Li–K–Cs electrolytes in Nyquist plots.
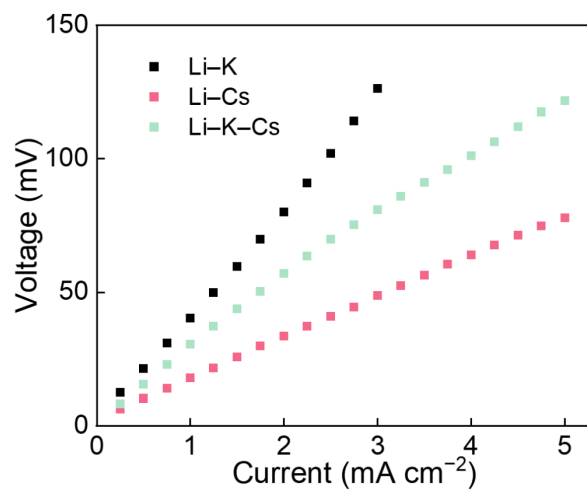
Fig. S8 Overpotential values of Li/Li cells at various current densities.
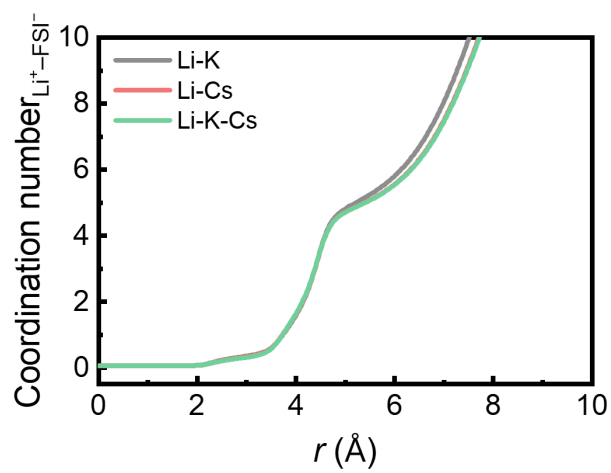
Fig. S9 Coordination numbers of FSI$^-$ around Li$^+$.
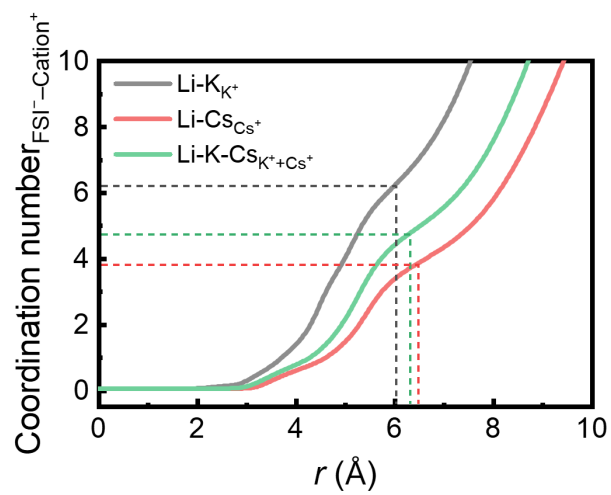
Fig. S10 Coordination numbers of K^+, Cs^+, or K^+ and Cs^+ around FSI^-.
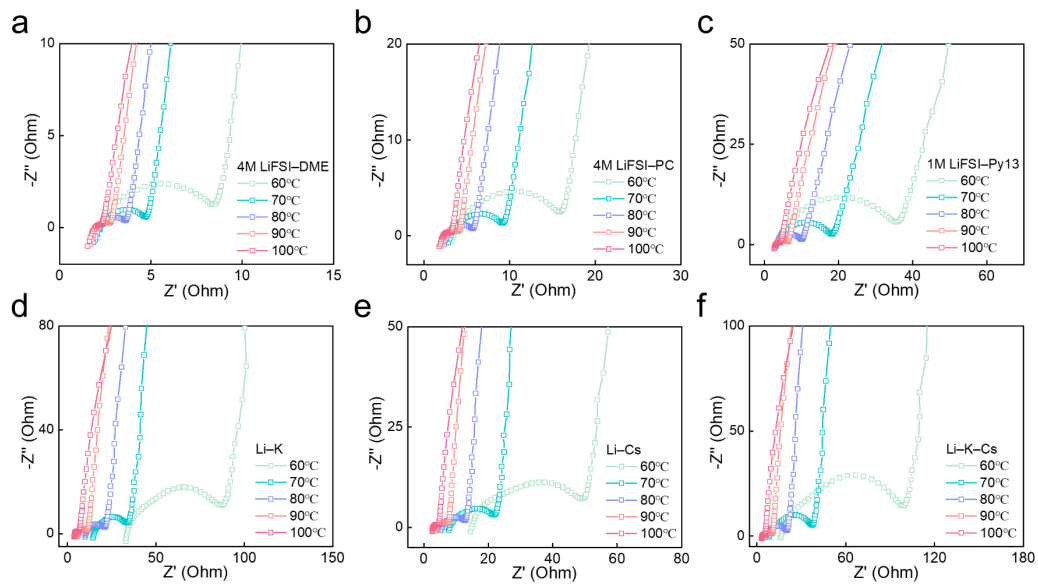
Fig. S11 Temperature-dependent impedance of NCM811/Li cells with (a) 4M LiFSI–DME, (b) 4M LiFSI–PC, (c) 1M LiFSI–Py13, (d) Li–K, (e) Li–Cs, and (f) Li–K–Cs electrolytes in Nyquist plots.
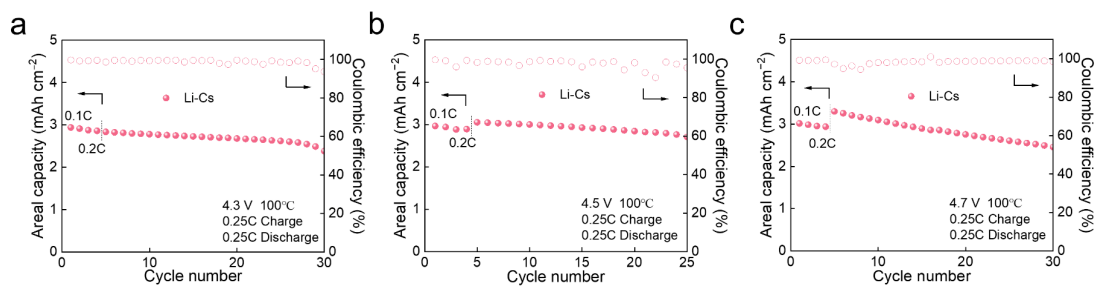
Fig. S12 The cycling performance of NCM811/Li cells at 100°C with cut-off voltages of (a) 4.3 V, (b) 4.5 V, and (c) 4.7 V.

Note: The NCM811/Li cells were firstly cycled at 0.1 C for two cycles and 0.2 C for two cycles with a cutoff voltage of 4.3 V for activation. Subsequently, the cells were subjected to galvanostatic cycling with varying cutoff voltages.
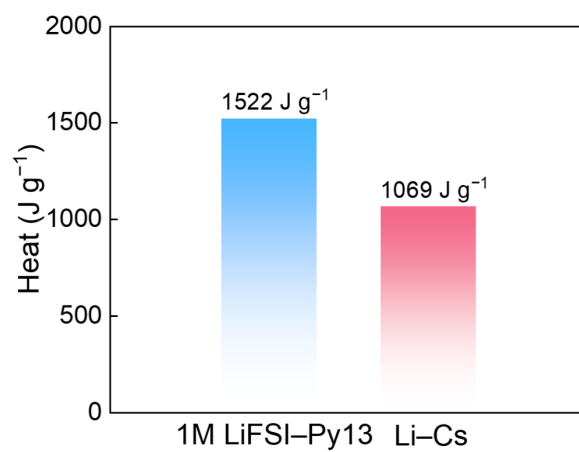
Fig. S13 The heat release of 1M LiFSI–Py13 and Li–Cs electrolytes.
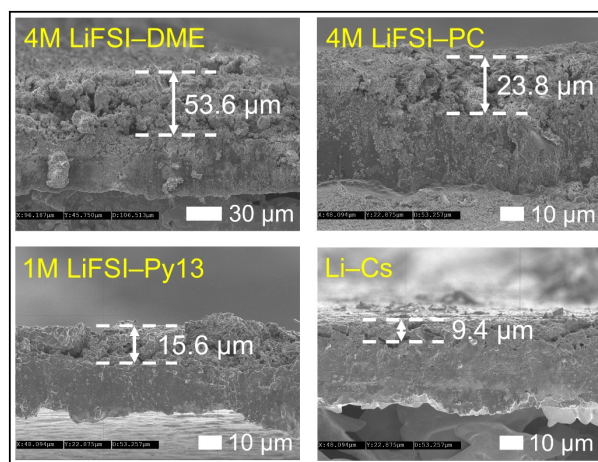
Fig. S14 Cross-section views of 0.5 mAh cm^{-2} Li deposition on Cu foils after 50 cycles.
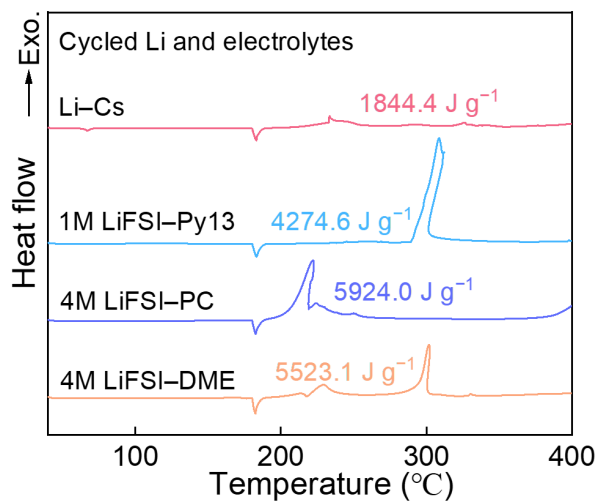
Fig. S15 DSC curves of the cycled Li metal and different electrolytes.
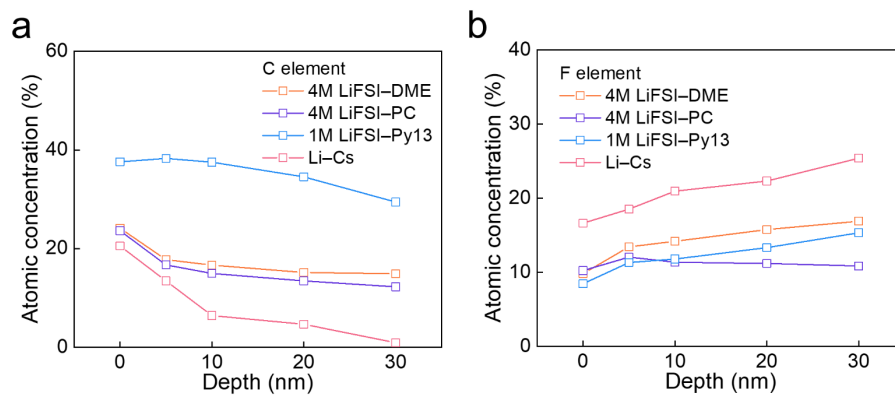
Fig. S16 The atomic concentration of (a) C element and (b) F element at different depth.
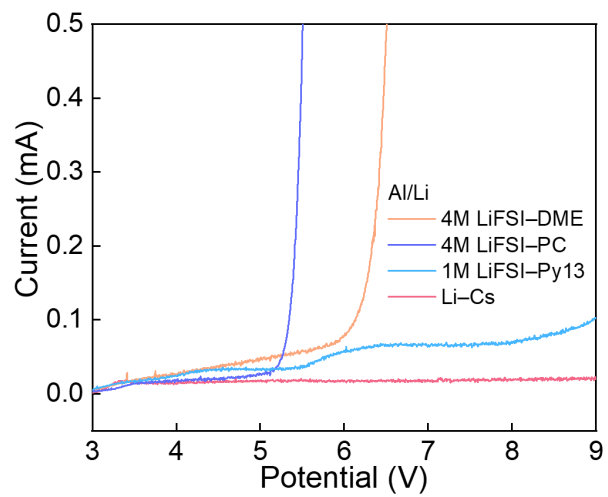
Fig. S17 LSV curves of electrolytes at a scan rate of 5 mV s^{-1}.
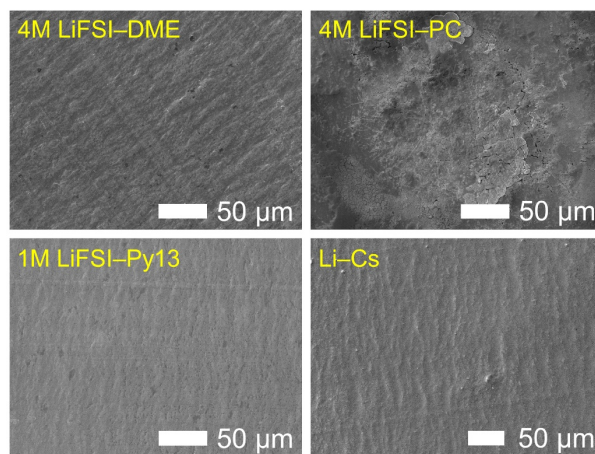
Fig. S18 SEM images of tested Al electrodes recovered from the Al/Li cells.
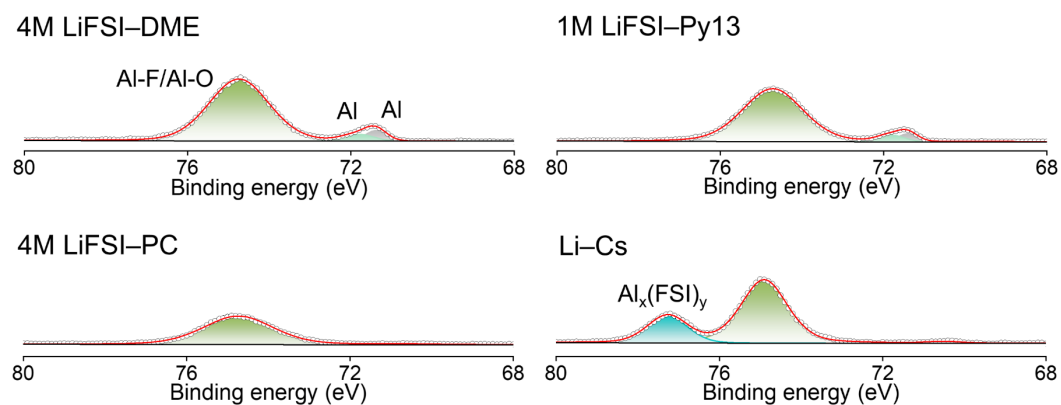
Fig. S19 Al 2p XPS spectra of the Al electrodes recovered from the Al/Li cells after 10 h chronoamperometry test at 4.5 V.

Note: When Al current collectors are polarized at high anodic potentials, Al and Al_2O_3 surface layer are oxidized to Al^{3+} ions, which react with FSI^- anions in electrolytes to form $Al(FSI)_3$ complexes. If these complexes are soluble in electrolytes, they diffuse into the electrolytes and continuously corrode the Al current collector. If these complexes are insoluble in electrolytes, they deposit on the Al surface and prevent further corrosion behavior. Therefore, the Al corrosion behavior in LiFSI-based electrolytes is highly associated with the different solubility of $Al(FSI)_3$ species in electrolytes.[16] As shown in Fig. S19, the Al electrodes after chronoamperometry test were analyzed by XPS. Compared to 4M LiFSI–DME and 1M LiFSI–Py13, the Al electrode that suffered severe corrosion in 4M LiFSI–PC shows less Al-F/Al-O species, indicating that the Al surface layer was damaged. A high content of Al^{3+} ions (44.40 ppm) was also verified in the residual electrolyte by ICP-OES in Table S8. This result means that $Al(FSI)_3$ has good solubility in PC solvents with a high dielectric constant, continuously exacerbating the Al corrosion. In sharp contrast, a large amount of $Al_x(FSI)_y$ species deposit on the Al surface in Li–Cs electrolyte and no Al^{3+} ions (0.00 ppm) were detected in the residual electrolyte, suggesting that the Li–Cs electrolyte has poor solubility for $Al_x(FSI)_y$ products, thereby inhibiting anodic corrosion to Al current collectors.
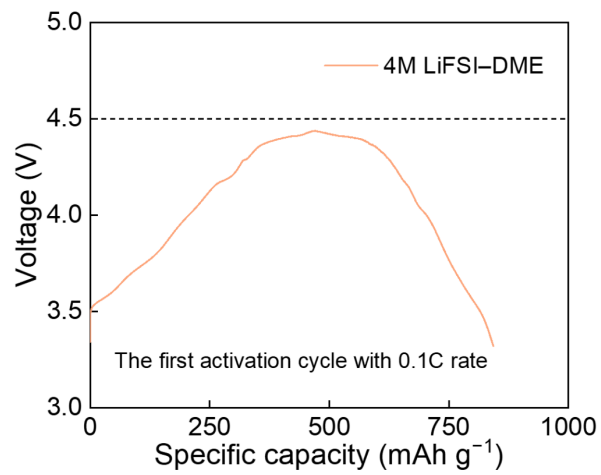
25

Fig. S20 The overcharging behavior of the NCM811/Li cell using 4M LiFSI–DME electrolyte.
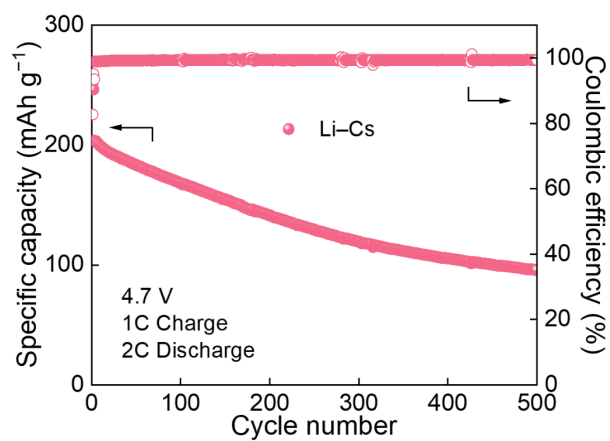
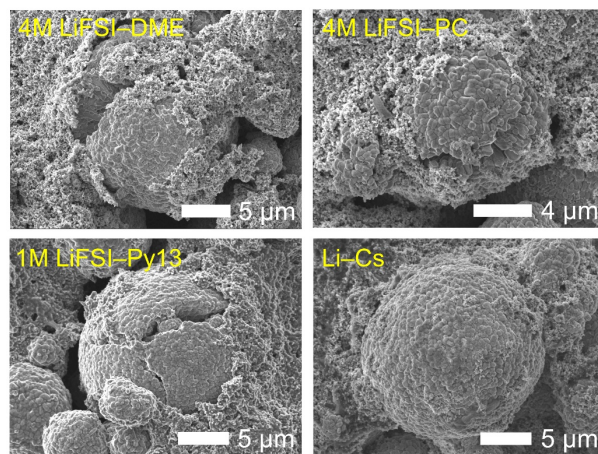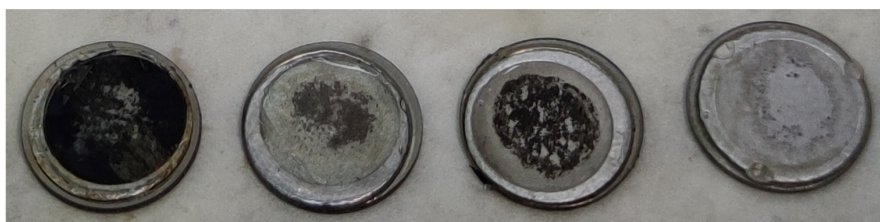**Fig. S21** The cycling performance of NCM811/Li cells using Li–Cs electrolyte at 4.7 V.

Fig. S22 SEM images of cycled NCM811 particles in different electrolytes.

4M LiFSI–DME   4M LiFSI–PC   1M LiFSI–Py13   Li–Cs

Fig. S23 Optical images of the cycled Li metal anodes in different electrolytes.
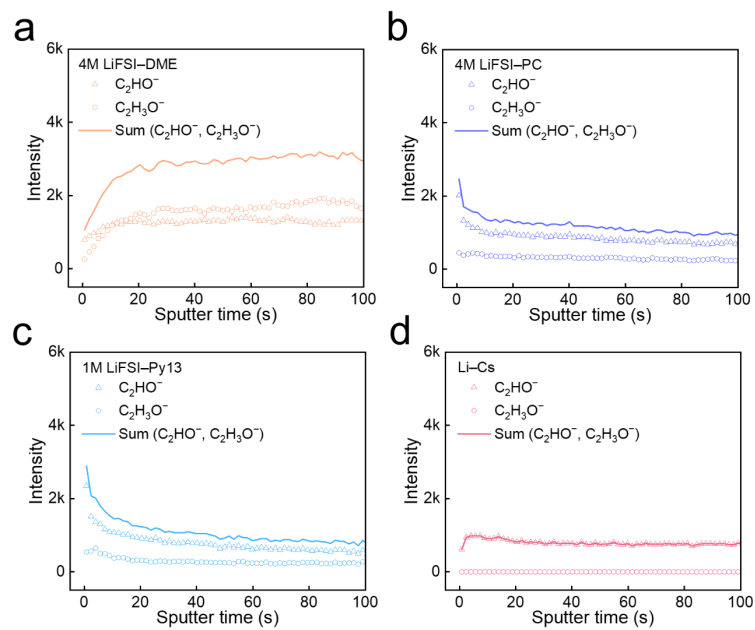
Fig. S24 TOF-SIMS depth profiles of organic species C_2HO^- and $C_2H_3O^-$ for cycled NCM811 cathodes in different electrolytes.
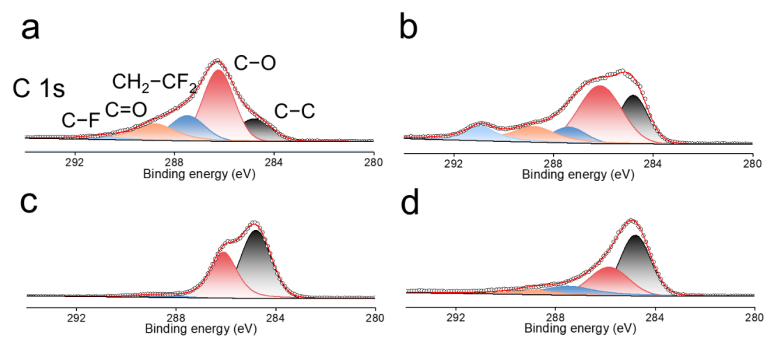
Fig. S25 XPS C 1s spectra results of CEI on the NCM811 surface in (a) 4M LiFSI–DME, (b) 4M LiFSI–PC, (c) 1M LiFSI–Py13 and (d) Li–Cs electrolytes.

Electrolyte system	Concentrated ether electrolyte (4M LiFSI–DME)		Concentrated ester electrolyte (4M LiFSI–PC)		Ionic liquid electrolyte (1M LiFSI–Py13)		Molten salt electrolyte (Li–Cs)	
Non-flammability (SET)	Poor $145\ s\ g^{-1}$	🚫	Poor $136\ s\ g^{-1}$	🚫	Good $0\ s\ g^{-1}$	✅	Good $0\ s\ g^{-1}$	✅
Thermal stability (Heat release temperature)	Poor 185℃	🚫	Moderate 190℃	⊖	Good 280℃	✅	Good 301℃	✅
Compatibility with Li metal (CE)	Unstable < 60%	🚫	Unstable < 80%	🚫	Unstable < 90%	🚫	Stable 98.8%	✅
Against Al corrosion (Leakage current)	Moderate 4 µA	⊖	Poor > 100µA	🚫	Moderate 2 µA	⊖	Good < 0.3 µA	✅
Oxidative stability	Poor 4.5 V	🚫	Moderate 4.7 V	⊖	Moderate 4.9 V	⊖	Good > 6.1 V	✅
Battery performance (70% retention)	Poor 0 cycle	🚫	Moderate 150 cycles	⊖	Poor 35 cycles	🚫	Good 300 cycles	✅

Fig. S26 Summary of drawbacks and advantages of different electrolytes studied in this work.

Table S1. Summary of resistance values of electrolytes at different temperatures.

Electrolytes	Resistance of electrolytes (SS/SS cells)/Ohm					
	50°C	60°C	70°C	80°C	90°C	100°C
4M LiFSI–DME	0.80	0.70	0.62	0.58	0.55	/
4M LiFSI–PC	2.14	1.70	1.43	1.27	1.18	/
1M LiFSI–Py13	1.00	0.86	0.75	0.67	0.63	/
Li–K	/	23.10	11.00	5.59	3.50	2.20
Li–Cs	/	11.16	6.05	3.70	2.54	1.90
Li–K–Cs	/	9.05	4.70	2.83	1.80	1.35

Table S2. Summary of the ionic conductivities and Li^+ transference numbers of three electrolytes.

Electrolyte	Total conductivity (mS cm^{-1})	Li^+ transference number	Li^+ conductivity (mS cm^{-1})	Temperature (°C)
Li–K	1.19	0.45	0.54	80
Li–Cs	1.79	0.53	0.95	80
Li–K–Cs	2.34	0.32	0.75	80

Table S3. Summary of interfacial resistance values of Li/Li cells at different temperatures.

Electrolytes	Interfacial resistance of Li/Li cells/Ohm				
	60°C	70°C	80°C	90°C	100°C
4M LiFSI–DME	28.2	14.2	6.9	4.2	1.1
4M LiFSI–PC	16.3	8.1	4.3	2.1	1.5
1M LiFSI–Py13	76.2	36.5	17.3	8.2	3.6
Li–K	31.9	12.5	5.0	2.2	0.8
Li–Cs	19.9	8.0	3.4	1.3	0.6
Li–K–Cs	40.0	15.1	6.3	2.9	0.7

Table S4. The tracer and charge conductivities of three electrolytes and their corresponding reciprocal of Haven ratio.

Electrolyte	Tracer (mS cm^{-1})	Charge (mS cm^{-1})	Reciprocal of Haven ratio
Li–K	0.45	0.30	0.67
Li–Cs	0.66	1.73	2.61
Li–K–Cs	1.75	1.82	1.04

Table S5. Summary of interfacial resistance values of NCM811/Li cells at different temperatures.

Electrolytes	Interfacial resistance of NCM811/Li cells/Ohm				
	60°C	70°C	80°C	90°C	100°C
4M LiFSI–DME	6.2	2.7	1.6	0.7	0.4
4M LiFSI–PC	13.5	6.9	3.2	1.8	1.1
1M LiFSI–Py13	36.7	15.8	7.4	3.5	1.4
Li–K	61.4	22.0	11.6	5.7	2.8
Li–Cs	40.0	16.5	8.3	4.0	2.1
Li–K–Cs	93.6	31.4	15.3	6.3	2.3

Table S6. Comparison of our work with previously reported molten salts.

Electrolyte	Cathode material	Areal capacity (mAh cm^{-2})	Cycling rate (C)	Refs.
Li$_{0.4}$Cs$_{0.6}$[fTfN]	LiFePO$_4$	0.15	1	17
	LiCoO$_2$	0.25	1	
Li$_{0.41}$K$_{0.59}$FSI	LiFePO$_4$	0.7	1	18
45wt%LiFSI–45wt%CsTFSI–10wt%LiTFSI	LiNi$_{0.8}$Co$_{0.15}$Al$_{0.05}$O$_2$	2	0.25	19
Li$_{0.30}$K$_{0.35}$Cs$_{0.35}$FSI	NCM811	1.66	0.33	20
Li–Cs	NCM811	2	1	This work

Table S7. Comparison of our work with recently reported publications.

Electrolyte	NCM811 loading (mg cm^{-1})	Cycle	Temperature (°C)	Refs.
1M LiPF$_6$ EC–EMC–PS	4	200	45	21
1M LiPF$_6$ EC–EMC–DMC–PTS	2	100	50	22
3.25M LiTFSI–0.1M LiClO$_4$ SL–TTE	2.5	100	55	23
1M LiPF$_6$ FEC–BTC	8.25	149	55	24
1.5M LiFSI DMOTFS	8	80	60	25
0.8M LiDFOB–0.2M LiPF$_6$–EC–EMC	2.5	100	60	26
1M LiPF$_6$ EC–EMC–DMC–LiHMDS	10	100	60	27
1M LiFSI EGDBE/TTE	5	200	60	28
	10	140	60	
Li–Cs	14	280	80	This work

Table S8. Comparison of the content of Al^{3+} dissolution in different electrolytes.

Electrolyte	Al dissolution/ppm
4M LiFSI–DME	0.10
4M LiFSI–PC	44.40
1M LiFSI–Py13	1.75
Li–Cs	0.00

Note: To detect the dissolution concentration of Al^{3+} ions in the electrolyte, the Al foil, separator and Li counter electrode after the chronoamperometry test were all thoroughly soaked in 3 mL EMC. Then, the resulting EMC solution was collected and sent to ICP-OES test. The obtained concentration values are based on the per gram of the above solutions.

Table S9. Comparison of the content of transition metal ions dissolution in different electrolytes.

Electrolyte	Ni dissolution/ppm	Co dissolution/ppm	Mn dissolution/ppm
4M LiFSI–DME	2.60	0.17	0.45
4M LiFSI–PC	1.88	0.15	0.31
1M LiFSI–Py13	0.64	0.09	0.07
Li–Cs	0.38	0.05	0.05

Note: NCM811/Li half cells with four different electrolytes were assembled and cycled at 1 C for 50 cycles at 80°C. To detect the concentration of transition metal ions (Ni^{2+}, Co^{2+} and Mn^{2+}) in the residual electrolyte, the cycled NCM811 cathode, separator and Li counter electrode were all thoroughly soaked in 3 mL EMC. Then, the resulting EMC solution was collected and sent to ICP-OES test. The obtained concentration values are based on the per gram of the above solutions. As shown in Table S9, the Ni dissolution content is much higher than that of Co and Mn in all four electrolytes. The 4M LiFSI–DME shows the highest Ni dissolution value of 2.60 ppm, which is due to the severe and continuous overcharging behavior occurred in the first cycle (Fig. S20). The Ni dissolution content in 4M LiFSI–PC (1.88 ppm) is approximately three times that in 1M LiFSI–Py13 (0.64 ppm). As for the Li–Cs molten salt electrolyte, it shows the lowest Ni dissolution value of 0.38 ppm, indicating that the structural collapse and transition metal escaping of NCM811 cathode have been effectively suppressed during high-temperature cycling.

References

1   P. Steve, *J. Comput. Phys.*, 1995, **117**, 1–19.

2   W. L. Jorgensen, D. S. Maxwell, J. Tirado-Rives, *J. Am. Chem. Soc.*, 1996, **118**, 11225–11236.

3   G. A. Kaminski, R. A. Friesner, *J. Phys. Chem. B*, 2001, **105**, 6474–6487.

4   K. P. Jensen, W. L. Jorgensen, *J. Chem. Theory Comput.*, 2006, **2**, 1499–1509.

5   J. N. Canongia Lopes, K. Shimizu, A. A. H. Pádua, Y. Umebayashi, S. Fukuda, K. Fujii, S.-i. Ishiguro, *J. Phys. Chem. B*, 2008, **112**, 9449–9455.

6   L. Martinez, R. Andrade, E. G. Birgin, J. M. Martinez, *J. Comput. Chem.*, 2009, **30**, 2157–2164.

7   K. Momma, F. Izumi, *J. Appl. Crystallogr.*, 2011, **44**, 1272–1276.

8   M. Parrinello, A. Rahman, *J. Appl. Phys.*, 1981, **52**, 7182–7190.

9   W. G. Hoover, *Phys. Rev. A*, 1985, **31**, 1695–1697.

10   S. Nose, *Mol. Phys.*, 1984, **52**, 255–268.

11   J. Evans, C. A. Vincent and P. G. Bruce, *Polymer*, 1987, **28**, 2324–2328.

12   K. Kubota, T. Nohira and R. Hagiwara, *Electrochim. Acta.*, 2012, **66**, 320–324.

13   T. N. Keigo Kubota, Rika Hagiwara, *J. Chem. Eng. Data*, 2010, **55**, 3142–3146.

14   J. Yu, W. Zhai, C. Zhang, C. Wu, R. Wei, S. Chen, Y. He, Q. Hu, Y. Yu and W. Liu, *ACS Energy Lett.*, 2023, **8**, 1468–1476.

15   R. Yunis, G. M.A. Girard, X. Wang, H. Zhu, A. J. Bhattacharyya, P. Howlett, D. R. MacFarlane, M. Forsyth, *Solid State Ionics*, 2018, **327**, 83–92.

16   K. Hirata, T. Kawase, Y. Sumida, *J. Electrochem. Soc.*, 2020, **167**, 140534.

17   K. Kubota and H. Matsumoto, *J. Electrochem. Soc.*, 2014, **161**, 902–907.

18   F. Xu, C. Liu, W. Feng, J. Nie, H. Li, X. Huang and Z. Zhou, *Electrochim. Acta*, 2014, **135**, 217–223.

19   A. L. Phan, C. Jayawardana, P. M. L. Le, J. Zhang, B. Nan, W. Zhang, B. L. Lucht, S. Hou and C. Wang, *Adv. Funct. Mater.*, 2023, **33**, 2301177.

20 M. C. Vu, P. Mirmira, R. J. Gomes, P. Ma, E. S. Doyle, H. S. Srinivasan and C. V. Amanchukwu, *Matter*, 2023, **6**, 4357–4375.

21 W.-C. Zheng, C.-G. Shi, P. Dai, Z. Huang, J.-X. Lin, H. Chen, M.-L. Sun, C.-H. Shen, C.-X. Luo, Q. Wang, X. Feng, Y.-M. Wei, L. Huang and S.-G. Sun, *J. Mater. Chem. A.*, 2022, **10**, 21912–21922.

22 Y. Cao, N. Li, K. Yuan, N. Li, W. Zhang, S. Liang, Z. Hou, D. Lei, T. Jin, J.-G. Wang, K. Xie and C. Shen, *Energy Storage Mater.*, 2023, **60**, 102851.

23 Y. Zhu, S. He, J. Ding, G. Zhao and F. Lian, Nano Research, 2022, 16, 3855–3863.

24 P. Xiao, Y. Zhao, Z. Piao, B. Li, G. Zhou and H.-M. Cheng, *Energy Environ. Sci.*, 2022, **15**, 2435–2444.

25 Z. Piao, X. Wu, H.-R. Ren, G. Lu, R. Gao, G. Zhou and H.-M. Cheng, *J. Am. Chem. Soc.*, 2023, **145**, 24260–24271.

26 D. Feng, S. Chen, R. Wang, T. Chen, S. Gu, J. Su, T. Dong and Y. Liu, *J. Electrochem. Soc.*, 2020, **167**, 110544.

27 D. Zhang, M. Liu, J. Ma, K. Yang, Z. Chen, K. Li, C. Zhang, Y. Wei, M. Zhou, P. Wang, Y. He, W. Lv, Q.-H. Yang, F. Kang and Y.-B. He, *Nat. Commun.*, 2022, **13**, 6966.

28 Z. Wang, C. Chen, D. Wang, Y. Zhu and B. Zhang, *Angew. Chem. Int. Ed.*, 2023, **62**, e202303950.